Optical properties of remotely doped AlAs/GaAs coupled quantum wire arrays.
I. Periodic quantum confinement and localization of minority carriers

T. Mélin[1,2,*] and F. Laruelle[1,†]

[1]*Laboratoire Photonique et Nanostructures, Centre National de la Recherche Scientifique, 196 Avenue Henri Ravera,
BP 107, 92225 Bagneux Cedex, France*
[2]*Institut d'Electronique et de Microélectronique du Nord, Centre National de la Recherche Scientifique, Avenue Poincaré,
BP 69, 59652 Villeneuve d'Ascq Cedex, France*

We perform low-temperature optical experiments on remotely doped lateral superlattices epitaxially grown on vicinal GaAs substrates. This quantum wire system provides a degenerate electron gas of density $n_s \simeq 8 \times 10^{11}$ cm^{-2} subjected to a tunable one-dimensional periodic potential of amplitude $\simeq 20$ meV and period $\simeq 30$ nm, i.e., at the scale of its Fermi energy ($E_F \simeq 25$ meV) and Fermi wavelength ($\lambda_F \simeq 30$ nm). We show that the one-dimensional quantum confinement strongly affects both photoluminescence and photoluminescence excitation properties of the degenerate electron system. Through a careful analysis of the optical emission and absorption linear polarization spectra together with their temperature dependence, we distinguish between features due to (i) the periodic one-dimensional confinement and (ii) the localization anisotropy of photocreated valence-band carriers.

I. INTRODUCTION

Much attention has been paid to the physics of one-dimensional (1D) semiconductor structures in the last decade. The experimental investigation of quantum wire (QWR) properties has been made possible by the appearance of reliable fabrication techniques based on various approaches such as etching and single-step or multistep epitaxial growth.[1] A strong emphasis has been put on the optical studies of nonintentionally doped QWR's such as *T* wires, *V* wires, and lateral superlattices (LSL's), where the excitonic regime looks now well understood.[2]

Doped QWR's providing clean 1D degenerate electron gases (DEG's) would be of considerable interest as well to test theoretical predictions in the 1D limit. For instance, optical spectra are predicted to be drastically altered by phase-space restrictions in Coulomb diffusion processes, with the appearance of power-law divergences at the Fermi edges, a phenomenon known as Fermi-edge singularities.[3] Also, the tunability of confinement in semiconductor structures enables us to probe the dimensionality transition towards 1D systems,[4] where the absence of quasiparticles at the Fermi level has been recently demonstrated experimentally by photoemission spectroscopy on quasi-1D organic salts.[5]

However, only few optical studies have been devoted to doped semiconductor QWR structures. Existing data refer mainly to type-II structures,[6] where electrons and holes are spatially separated, to 1D plasmon modes in etched wires studied by Raman optical spectroscopy,[7] and to dense 1D electron-hole plasmas generated by bringing undoped QWR's under strong optical excitation.[8] This underlines that the doping of QWR structures remains in most cases a technological issue.

Here, we report on remotely doped AlAs/GaAs QWR's known as LSL's. The 1D confinement is achieved inside the channel of a 2D heterostructure by self-organized molecular beam epitaxy (MBE) growth, as demonstrated by Petroff *et al.* in the 1980's.[9] Due to the one-step growth scheme, LSL's can be remotely doped as easily as in 2D,[10] with a density (here $n_s \simeq 8 \times 10^{11}$ cm^{-2}) controlled by the thickness of the spacer layer between dopants and the LSL. The 1D potential amplitude ($\simeq 20$ meV) and period ($\simeq 30$ nm) (Ref. 11) closely match the Fermi energy (25 meV) and Fermi wavelength ($\simeq 30$ nm) of the electron system, so that strong evidence for 1D quantum confinement is expected in both transport and optical properties. Indeed, magnetotransport experiments have revealed striking properties such as the spin polarization of Landau bands at high magnetic fields.[12]

In the present paper, we focus on the optical properties of remotely doped LSL's. First, we review the LSL fabrication and the tunability of their electronic properties with tilt, and describe the basic optical processes involved in low-temperature photoluminescence (PL) and photoluminescence excitation (PLE) experiments on a 2D DEG. We then turn to 1D-modulated DEG's achieved by remote doping of LSL's, and analyze their PL and PLE linear polarization spectra. This reveals that the LSL optical properties are not only governed by periodic quantum confinement, but also by the localization anisotropy of photocreated valence carriers within one LSL period. Features associated with the former and the latter contributions are distinguished experimentally by their temperature dependence. The analysis brings an experimental identification of the nature of optical processes involved in the PLE onset of absorption below the Fermi threshold for direct transitions. The final facet of LSL optical properties consists in the Fermi-edge singularities which develop in the regime of periodic intersubband couplings.[13] The analysis of these aspects in terms of Fano resonances[14] is in fact general to semiconductor heterostructures and not restricted to QWR systems: it therefore makes the scope of a separate paper.[15]
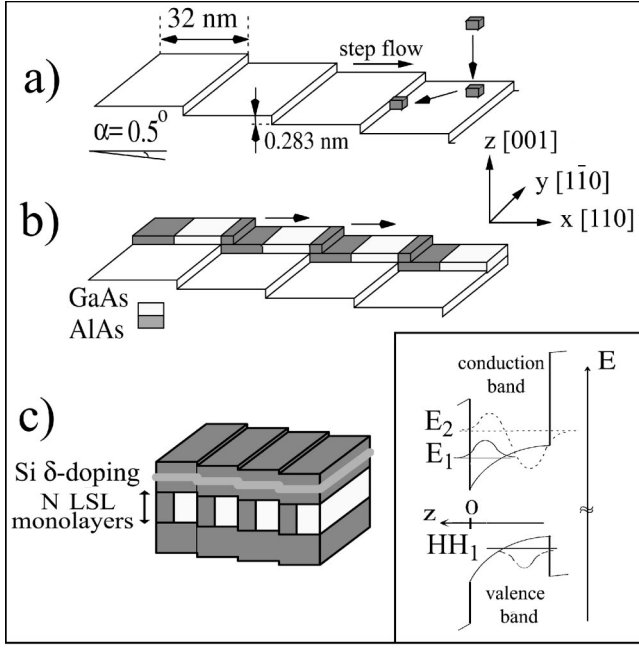
FIG. 1. (a) Schema of a GaAs vicinal surface (misorientation angle $\alpha = 0.5°$) exhibiting a monomolecular step array (period $L_x = 32$ nm) in the step-flow mode. (b) During the epitaxy of each LSL monolayer, AlAs and GaAs are sequentially grown, so as to induce the lateral confinement. (c) The stacking of N LSL monolayers is embedded between $Al_{0.33}Ga_{0.67}As$ barriers, with remote Si δ doping on the surface side of the structure. Inset: asymmetric confinement in a remotely doped 2D QW. The conduction and valence envelope functions of E_1, E_2, and HH_1 are depicted.

II. SAMPLES AND EXPERIMENTS

Samples are grown by MBE on 0.5° vicinal GaAs (001) substrates, which exhibit a monomolecular step array of periodicity $L_x = 32$ nm [see Fig. 1(a)] after the growth of a GaAs buffer layer in the step-flow mode.[16] This step array is used to laterally organize the growth, each LSL layer consisting in a monolayer fraction $x_{Al} \simeq 0.07$ of AlAs followed by a fraction $x_{Ga} \simeq 0.93$ of GaAs [Fig. 1(b)]. The N-monolayer-thick LSL ($55 \leq N \leq 71$) is inserted between two $Al_{0.33}Ga_{0.67}As$ barriers, and remote Si δ doping is achieved on the surface side [see Fig. 1(c)], leading to an electron density $n_s \simeq 8 \times 10^{11}$ cm^{-2} at 2 K under optical illumination for a 9 nm spacer layer thickness.

In Fig. 1 the LSL is clearly drawn in an idealized view with pure GaAs and AlAs stripes. Experimentally, the amplitude of the 1D periodic potential is strongly weakened both in the conduction and valence bands by growth factors such as the aluminum-gallium vertical segregation during MBE growth or the disorder of the vicinal surface step array. This has been quantitatively analyzed previously and corresponds to a $\simeq 90\%$ reduction of the effective periodic confinement amplitude in LSL's with a low alloy concentration.[17] In the case of remotely doped structures, the effective LSL potential is further screened by the electrostatic potential induced by the periodically confined degenerate electron system itself. This phenomenon, however, differs from the Al/Ga segregation and step-array disorder effects, since it opposes the
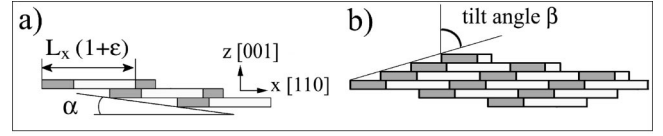

FIG. 2. (a) Excess coverage of the LSL terraces for a total AlAs and GaAs coverage ratio $x_{Al} + x_{Ga} > 1$. The excess coverage ratio ε equals $x_{Al} + x_{Ga} - 1$. (b) Geometrical tilt angle β of the LSL. β is linked to ε by $\tan \beta = \varepsilon / \alpha$.

conduction-band confinement potential, while it emphasizes the valence-band one. In the conduction band, the corresponding reduction factor can reach 30% of the 1D potential in low-density samples ($n_s \simeq 4.5 \times 10^{11}$ cm^{-2}), in good agreement with self-consistent Schrödinger-Poisson numerical calculations.[18]

Throughout this paper, we will phenomenologically account for the growth and static-screening phenomena by referring to the effective 1D confinement potential probed by 2D conduction-band electronic states. Limiting our description to the first Fourier component of the 1D confinement, the confinement potential reads

$$V_{1D}(x) = V_{1D} \cos\left(\frac{2\pi x}{L_x} \right).$$

From previous work,[4,11,12] we expect $2V_{1D} \simeq 20$ meV. As pointed out in the Introduction, the LSL effective potential amplitude and period closely match the Fermi energy (25 meV) and Fermi wavelength ($\lambda_F \simeq 30$ nm) of the electron system. This shows that the DEG is close to the 1D quantum limit, a few 1D minibands only being populated by degenerate electrons.

Up to this point, we described the situation where the total fluxes of AlAs and GaAs are adjusted to cover exactly the terrace width during each MBE cycle ($x_{Al} + x_{Ga} = 1$). However, the total coverage varies along the samples due to flux gradients of effusion cells in the MBE chamber ($x_{Al} + x_{Ga} = 1 + \varepsilon$). This induces a phase shift between each LSL monolayer:

$$V_{1D}(x,z) = V_{1D} \cos\left(\frac{2\pi x}{L_x} - 2\pi\varepsilon \frac{z}{a} \right).$$

where a is the monolayer thickness ($a = 2.83$ Å). Geometrically, the LSL stripes get tilted with an angle β with respect to the growth direction as sketched in Fig. 2. However, this structural parameter is inappropriate to describe the electronic properties of tilted LSL's. To do so, one rather needs to take into account the vertical extension of the 2D electronic states probing the LSL potential. The LSL tilt can be monitored at this scale by the phase shift $2\pi N\varepsilon$ of the LSL potential throughout the N LSL monolayers. We will thus adopt in the following $N\varepsilon$ as tilt parameter to describe the electronic properties of tilted LSL's. This quantity has in addition a practical meaning, since a $\Delta N\varepsilon = 1$ variation of the tilt parameter corresponds to an increase of the QW thickness N by one monolayer. Experimentally, we probe the LSL optical properties with a 40 μm laser spot moved along the sample as shown in the inset of Fig. 3, while ε values (i.e.,
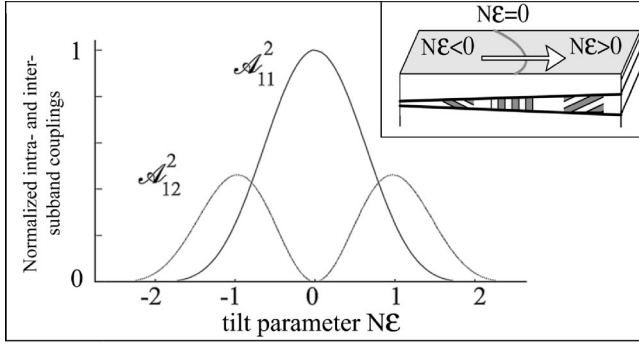
FIG. 3. Squared normalized intra- and intersubband couplings $\mathcal{A}_{11}^2$ and $\mathcal{A}_{12}^2$ as a function of the tilt parameter $N\varepsilon$ (see text). Inset: schematical sample side view showing how optical properties are tracked along a given wafer. The $N\varepsilon=0$ region (untilted LSL) corresponds to a line on the sample. Variations of the LSL thickness with tilt are also represented.

the x_{Al} and x_{Ga} fluxes) are measured independently from the LSL properties at each laser spot position with an accuracy $\Delta\varepsilon=4\times10^{-4}$, thanks to additional reference heterostructures buried below the LSL.[4]

The electronic properties of LSL's can be described as follows. For nontilted LSL's, the 1D periodic potential is separable between the [110] (x) and growth (z) directions. It acts therefore only within each 2D-confined conduction subband E_n, by coupling with an amplitude $V_{1D}/2$ in-plane states $\mathbf{k}=(k_x,k_y)$ and $\mathbf{k}'=(k_x',k_y')$ such as $k_x'-k_x=\pm2\pi/L_x$ and $k_y'=k_y$. In the case of tilted LSL's, the LSL potential is no more separable between x and z, so that the symmetries of the 1D confinement potential are changed, giving rise to additionnal intersubband periodic couplings acting between states $\mathbf{k}$ and $\mathbf{k}'=(k_x\pm2\pi/L_x,k_y)$ belonging to subbands E_m and E_n with different quantum numbers $m\neq n$. We characterize the intra- and intersubband coupling relative amplitudes as a function of tilt by the parameter A_{mn}:

$$\mathcal{A}_{mn}=\frac{2}{V_{1D}}\int\int\psi_m^*(z)V_{1D}(x,z)\psi_n(z)e^{i2\pi/L_x}dx\,dz,$$

where ψ_m (ψ_n) are the envelope functions in the two-dimensional subbands E_m (E_n). Obviously, $A_{mm}=1$ and $A_{mn}=0$ ($m\neq n$) for $N\varepsilon=0$, while A_{mn} ($m\neq n$) terms become nonzero for $N\varepsilon\neq0$. For the lowest indexes, we get[19]

$$\mathcal{A}_{11}=\frac{-1/\pi}{N\varepsilon(1-N^2\varepsilon^2)}\sin(\pi N\varepsilon),$$

$$\mathcal{A}_{12}=\frac{-4N\varepsilon/\pi}{(1-4N^2\varepsilon^2)(9-4N^2\varepsilon^2)}\cos(\pi N\varepsilon).$$

We have reported for illustration in Fig. 3 the squared amplitudes of $\mathcal{A}_{11}$ and $\mathcal{A}_{12}$. $\mathcal{A}_{11}^2$ almost monotonically vanishes with tilt: this parameter is directly proportional to the redshift of PL transitions in undoped LSL's (Refs. 4 and 11) in the range of validity of the perturbation theory. The limit where $\mathcal{A}_{11}^2\rightarrow0$ means that electrons fully average the tilted

LSL potential owing to their z extension: the tilted LSL acts almost as an alloy. The intersubband parameter $\mathcal{A}_{12}^2$ is zero for $N\varepsilon=0$. Due to the broken separability between the x and z axes, it raises when tilt is increased, but gets also averaged in the limit of large $N\varepsilon$ values. $\mathcal{A}_{12}$ thus displays a characteristic camelback shape, with a maximum amplitude for $N\varepsilon=1$. This behavior corresponds to the enhancement of Fermi-edge singularities in tilted remotely doped LSL's.[13]

The samples investigated in this paper are those of Ref. 13. Sample A (B) consists of a $N=71$ (55) monolayer thick LSL of mean $x_{Al}=7\%$ aluminum content inserted between $Al_{0.33}Ga_{0.67}As$ bariers. Remote Si δ doping is provided with a spacer layer thickness $\simeq9$ nm. We performed 4 K magneto-optical experiments[20] to measure Fermi energies and conduction- and valence-band electronic masses. For sample A, we get $E_F=26.5\pm0.4$ meV, $m_e=0.074m_0$ and $m_h=0.36m_0$, where m_0 denotes the free electron mass. In the case of sample B, we find $E_F=27.0\pm0.4$ meV, $m_e=0.074m_0$, and $m_h=0.28m_0$. Sheet densities extracted from these measurements equal $n_s\simeq8.3\times10^{11}$ cm^{-2}. Samples A and B are thus quite similar, except for the E_1-E_2 subband spacing due to the different LSL thickness. Indeed, the energy separation between the excitonic resonance associated with E_2 (E_{2_X}) and Fermi-level transitions equals 6.5 meV for sample A while it reaches 19.5 meV for sample B. This makes Fermi-edge singularity effects more pronounced for sample A compared to sample B.[13]

Photoluminescence and PL excitation experiments are performed at 1.8 K with the sample immersed in superfluid helium. The excitation is provided by a tunable Ti:Sa laser with a maximum 300 μW power focused within a 40 μm spot. The PL signal is dispersed by a double monochromator with a typical 0.1 meV resolution. A photomultiplier is used for detection, with a preamplifier enabling a counting dynamics over six order of magnitudes. PL and PLE linear polarizations are measured at a frequency between 50 kHz and 100 kHz using an acoustooptic modulator locked with a two-channel photon-counting setup.

III. OPTICAL EMISSION AND ABSORPTION OF A TWO-DIMENSIONAL ELECTRON GAS

We briefly review the basic mechanisms of optical emission and absorption of a 2D DEG in a semiconductor heterostructure. The DEG is described as a $T=0$ K Fermi sea, with conduction carriers filling states from zero in-plane wave vector up to the Fermi wave vector k_F ($k_F\simeq0.02$ Å^{-1} for samples A and B). We neglect the Coulomb interaction between valence holes and the Fermi sea and do not address in this section Fermi-edge singularity issues.

Experimentally, remotely doped QW's display a PL line shape with an asymmetrical tail towards high energies at low temperature [see Fig. 4(b)]. This shows that usual k-selection rules for direct optical processes[21] do not apply, because photocreated holes having relaxed at the top of the valence band would only allow $\mathbf{k}\simeq0$ wave-vector transitions and thus lead to a symmetrical PL profile. Indirect optical processes can take place in presence of remote ionized dopants as pointed out by Lyo, Jones and Klem.[22] Since the efficiency of remote
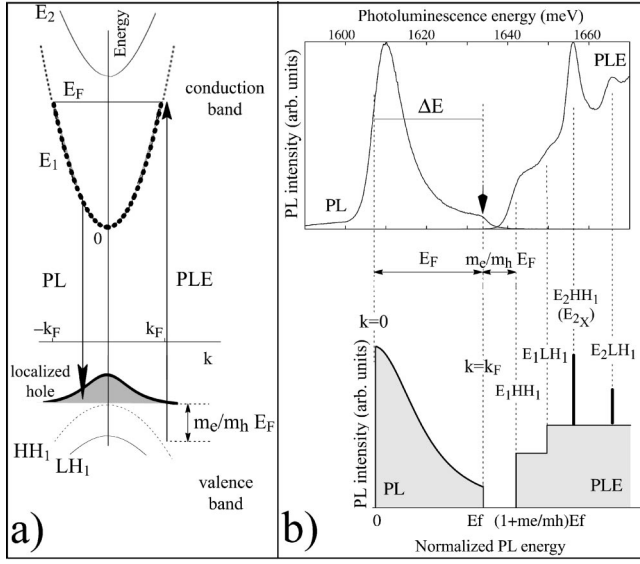
FIG. 4. (a) In-plane band-structure of the conduction and valence bands of a remotely doped QW at $T=0$ K. Dominant PL and PLE optical processes are depicted. In PL, conduction electrons recombine onto valence states localized on potential fluctuations at the top of the subband HH$_1$. In PLE, direct absorption processes start between HH$_1$ states and E_1 electrons with in-plane wave vectors greater than the Fermi wave vector k_F. (b) Comparison between the theoretical line shapes in emission and absorption with PL and PLE spectra of a 2D DEG (in fact sample B for $N\varepsilon\to\infty$). The PL line shape width ΔE equals the Fermi energy, while the PLE starts with an m_e/m_h ΔE shift (Moss-Burstein shift) with respect to the PL Fermi-edge cutoff. Excitonic resonances associated with the empty conduction subband E_2 appear as quasidiscrete levels in PLE.

dopant diffusions decreases strongly with the conduction wave vectors, the resulting PL oscillator strength decreases with energy, but allows transitions up to the DEG Fermi-level states at E_F, even for high electron densities such as ours ($n_s\simeq8\times10^{11}$ cm^{-2}). However, in the case of our samples, another indirect mechanism sets in, due to the ternary alloy composition $x_{Al}\simeq7\%$ inside the LSL. The associated disorder creates a band tail of localized states at the top of the HH$_1$ subband. In PL, photocreated holes relax on most localized states and get a k-space extension comparable to the Fermi wave vector k_F, thus allowing PL transitions for Fermi-sea electrons with wave vectors up to k_F [see Fig. 4(a)]. The validity of this scheme will be demonstrated below. In PLE, however, the valence-band population is not of importance and direct optical processes dominate over indirect ones. The direct absorption starts for wave vectors greater than the DEG Fermi wave vector due to the Pauli exclusion principle. Because of the finite hole mass, the corresponding absorption edge in PLE is blueshifted by m_e/m_h E_F with respect to the PL Fermi-edge cutoff, a quantity known as the Moss-Burstein shift. The empty subband E_2 gives rise to transitions of excitonic character as seen from the sharp resonances of E_2HH$_1$ (namely, E_{2_X}) and E_2LH$_1$ in the experimental PLE data of Fig. 4(b).

Localized states have been the subject of numerous stud-

ies in undoped QW's and QWR's recently,[23] mainly by means of PL studies at the μm scale in order to probe the emission of individually localized excitons. However, little work has been done in situations where only one of the two recombining electronic states is localized, as is the case in the PL of remotely doped LSL's. We demonstrate in the following that the localization of hole states in the valence-band tail can be probed using a conventional PL setup at a 40 μm scale.

IV. LOCALIZATION OF VALENCE HOLES

The theory developed by Halperin and Lax[24] can be used to describe the localization of valence holes in the potential fluctuations of a ternary alloy like Al$_x$Ga$_{1-x}$As. This variational method assumes a correspondence principle between the energy E of a localized state and its extension (or its shape) $\phi_E(\mathbf{r})$. The case of MBE-grown Al$_x$Ga$_{1-x}$ alloys corresponds to a high density of randomly positionned diffusion sites[21] for which a statistical description accounts for the disorder "seen" by the wave fuction ϕ_E. Then, the density of states $\rho_\phi(E)$—which has to be maximized with respect to ϕ in this variational scheme—reads[24]

$$\rho_{\phi_E}(E)=\mathcal{A}(E)\exp\left(\frac{-(E-\theta)^2}{2\sigma^2}\right),$$

where ϕ_E is the trial wave function at energy E, $\mathcal{A}$ a function slowly varying with energy E, θ the kinetic energy associated with ϕ, and σ the standard deviation of the statistical disorder potential seen by $\phi(\mathbf{r}-\mathbf{r}_0)$ when $\mathbf{r}_0$ is varied in the 2D space. Taking a parabolic hole dispersion $E=-\hbar^2k^2/2m^*$ and assuming a Gaussian 2D profile for the trial wave function,

$$\phi_E(\mathbf{r})=\sqrt{\frac{2}{\pi}}\frac{1}{\mu}\exp\left(-\frac{x^2+y^2}{\mu^2}\right),$$

one obtains a description of localized hole levels for $E>0$ with a characteristic extension

$$\mu(E)=\sqrt{\frac{3\hbar^2\pi}{2m^*E}}.$$

The associated band tail of the valence-band density of states is exponential: $\rho(E)\propto\exp(-E/E_c)$, with a characteristic localization energy

$$E_c=\frac{m^*a^2x(1-x)(\Delta V)^2}{3\pi^2\hbar^2},$$

where x is the alloy mean composition, a denotes the crystal lattice constant, and ΔV is the valence-band-gap offset between pure AlAs and GaAs materials.

The gradual localization of valence-band states with energy is depicted in Fig. 5. Taking $x=7\%$, $a=5.67$ Å, $\Delta V=0.5$ eV, and $m^*=0.35m_0$ for the HH$_1$ subband, one estimates $\mu\simeq32$ nm$/\sqrt{E}$ (E in meV) and $E_c\simeq0.8$ meV. Such parameters are well adapted to describe localization effects in actual MBE-grown structures with ternary alloys such as
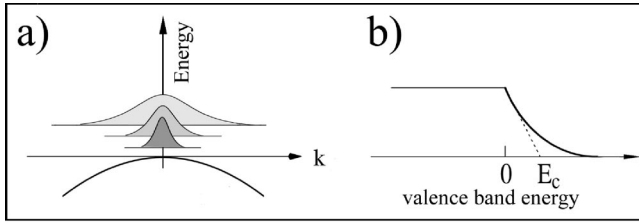
FIG. 5. (a) Localized states ($E>0$) in the valence band in presence of disorder. (b) Schema of the exponential valence-band tail with characteristic energy E_c (see text).

$Al_xGa_{1-x}As$ quantum wells, because (i) E_c corresponds to the usual Stokes shift values of our samples and (ii) $\mu(E=1$ meV) matches typical Fermi wavelengths in 2D DEG's. This underlines the efficiency of indirect PL recombination processes between delocalized DEG states and valence states localized by alloy disorder.

Such considerations show that the optical properties of lateral superlattices will be drastically affected by localization effects in the valence band. Indeed, since the typical localization length $\mu(E_c)$ is greater than the LSL period ($L_x=32$ nm) *while remaining of same order of magnitude*, 2D valence states localized by alloy disorder will easily get trapped within one LSL period in presence of the 1D confinement potential along the x direction. Strong PL linear polarization features can thus be expected in LSL's due to this anisotropic valence hole localization. Also, even if most localized valence states get anisotropically localized within one LSL terrace, this process gets rapidly inefficient for more delocalized states in the valence-band tail. The PL polarization features associated with anisotropically localized valence states will therefore vary strongly as a function of the localization length. This property will be used in the analysis of the optical properties of LSL's, so as to distinguish between features due on the one hand to the periodic one-dimensional confinement and on the other hand to the localization anisotropy of photocreated valence-band carriers. Experimentally, the localization length of valence carriers can be tuned by raising the sample temperature above the localization energy E_c. The experiments reported below will demonstrate the major role played by localized carriers in optical emission and absorption processes in the vicinity of the PL and PLE Fermi edges.

V. FROM QUANTUM WELLS TO COUPLED QUANTUM WIRE ARRAYS

We now focus on the optical properties of QWR arrays, using sample B at $N\varepsilon=0$, for which intersubband coupling effects can be neglected in a first approximation.

In Fig. 6 we show 2 K PL and PLE spectra, as well as their linear polarization spectra. We define a linear polarization ratio (LPR) as the difference between PL components having an electric field along the x ($[110]$) and along the y ($[1\bar{1}0]$) axes, normalized to the total PL intensity. At 2D, even if individual k transitions are polarized outside the Brillouin zone center due to valence-band mixing effects,[21] a DEG emission or absorption is not linearly polarized, be-
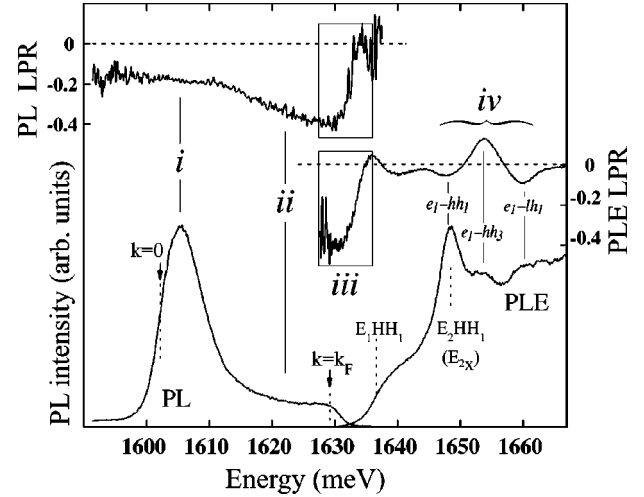

FIG. 6. PL, PLE and their linear polarization ratios for sample B at $N\varepsilon=0$. Features denoted by (i), (ii), (iii), and (iv) are described in following sections. In the PL spectrum, arrows labeled $\mathbf{k}=0$ and $\mathbf{k}=\mathbf{k_F}$ denote zone-center and Fermi-edge transitions as determined from magneto-optical measurements.

cause of the isotropy of conduction constant energy surfaces. As seen in Fig. 6 both PL and PLE of LSL's display well-structured LPR spectra. We will show that part of the structures are directly connected to the presence of the 1D *periodic* potential of the LSL. This corresponds to features labeled (i) (negative PL LPR for small wave-vector transitions) and (iv) (1D excitonic transitions associated with the empty subband E_2). Other features, i.e., (ii) the negative PL LPR for large wave-vector transitions and (iii) the Fermi-level depolarization in PL and PLE, will be attributed to the anisotropy of the valence-hole localization. The analysis is developed in the next sections, after a short analysis of 1D density of states (DOS) singularities in LSL's.

VI. ABSENCE OF VAN HOVE SINGULARITIES IN PHOTOLUMINESCENCE SPECTRA

It is striking in Fig. 6 that the PL line shape does not mirror the DOS singularities expected from the 1D confinement, as revealed, for instance, in scanning tunneling microscopy studies on carbon nanotubes.[25] They are calculated in Fig. 7 (bottom) for a typical $2V_{1D}=20$ meV modulation amplitude. Singular points labeled π/L_x^- (π/L_x^+) correspond to the first minigap states at $\mathbf{k}=(\pi/L_x,0)$ in the first (second) miniband. The same holds for $2\pi/L_x^-$ state ($2\pi/L_x^+$ state) associated with the second minigap states at $\mathbf{k}=(2\pi/L_x,0)$ in the second (third) miniband.

Clearly, one cannot refer to disorder to account for the absence of DOS singularities in experimental photoluminescence spectra, even if some of them (π/L_x^- and $2\pi/L_x^-$) appear as peaks due to their saddle-point character in the band structure[11] and could be easily washed out by the presence of disorder.

We rather propose an explanation of the absence of 1D DOS singularities in PL spectra in terms of the localization of valence holes. In a tilted LSL, the 2D model released in
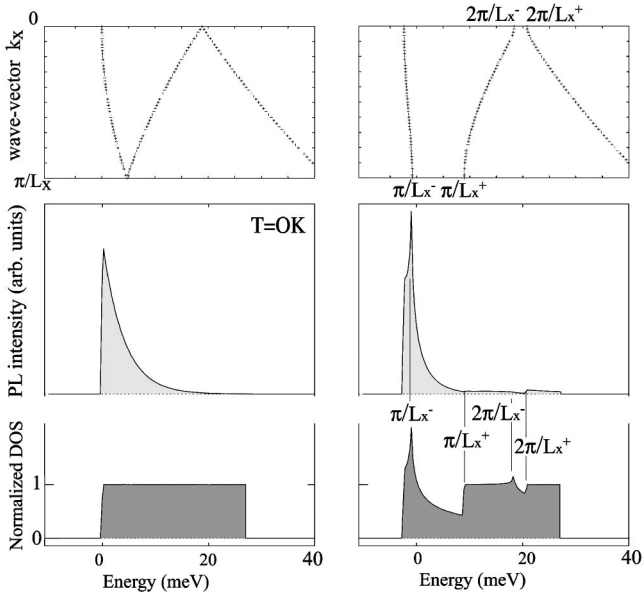
FIG. 7. Top: conduction dispersion laws in reduced zone scheme showing the formation of 1D minibands in the k_x direction for $V_{1D}=0$ (left) and $V_{1D}=10$ meV (right). Singular points labeled π/L_x^-, π/L_x^+, $2\pi/L_x^-$, and $2\pi/L_x^+$ appear as a result of the minigap openings in $(k_x,k_y)=(\pi/L_x,0)$, and $(2\pi/L_x,0)$. Bottom: calculated densities of states given in units of the 2D DOS. Middle: calculated optical spectra using an isotropically localized hole ($\Delta k_x=\Delta k_y=0.013$ Å^{-1}) for $V_{1D}=0$ and an anisotropically localized hole ($\Delta k_x=0.035$ Å^{-1}, $\Delta k_y=0.013$ Å^{-1}) for $V_{1D}=10$ meV. The spectra share the same vertical scale.

the previous section already predicts that valence states localize within one LSL period ($L_x \simeq 32$ nm) due to the alloy composition of the LSL. Therefore, for $N\varepsilon=0$, holes will localize inside individual LSL potential extrema, as sketched in Fig. 8. We have also plotted in Fig. 8 the symmetries of π/L_x^- and π/L_x^+ minigap states. Selection rules appear and predict that π/L_x^+ transitions should be optically inactive, in analogy with usual selection rules in a 2D QW [see Fig. 8(b)]. To ensure this, we calculated in Fig. 7 the corresponding PL spectrum. The DOS singularity associated with the second 1D miniband (π/L_x^+) is completely washed out. However, the steplike onset of the third 1D miniband
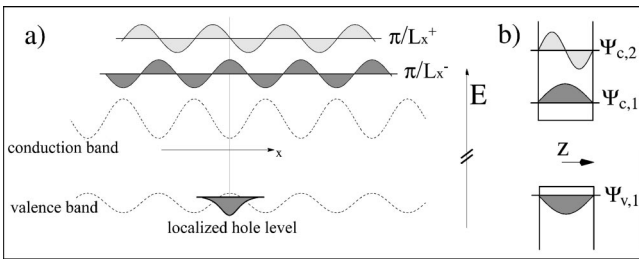

FIG. 8. (a) 1D confinement potential in conduction and valence bands (dotted lines). The minigap states π/L_x^- and π/L_x^+ and the valence hole states localized on a potential extremum are depicted. (b) First confined states in a nonintentionally doped QW. Symmetries are analogous to (a) and lead to similar optical selection rules for PL processes.

($2\pi/L_x^+$) should be resolved in PL experiments.

The absence of 1D DOS singularities remains thus partially unexplained, while the presence of a 1D periodic confinement is fully established in these samples.[13] Two speculative arguments can be mentionned which, however, go beyond the scope of this paper. The first one is that indirect processes associated with remote dopants[22] can be boosted via umklapp processes around 1D miniband edges in QWR's,[26] even if such processes are inefficient at the corresponding **k** wave vectors in 2D. Also, it has been shown that DOS singularities are suppressed because of the Coulomb interaction in undoped QWR's.[27] The comparison with our data is striking, even if the link with remotely doped structures is not straightforward.

VII. ONE-DIMENSIONAL EXCITONIC TRANSITIONS ASSOCIATED WITH E_2

As observed in Fig. 6, the E_2 subband splits into 1D excitonic structures labeled (iv) which are equivalent to those observed for E_1 in the PLE of undoped LSL's.[11]

They consist of the following: (a) a ground e_1-hh_1 transition between the first E_2 and HH$_1$ 1D minibands, with a characteristic negative LPR, (b) a e_1-hh_3 transition between the first E_2 miniband and the third lateral miniband of HH$_1$, correlated to a positive extremum in the PLE LPR, and (c) the ground light-hole e_1-lh_1 transition involving the first lateral minibands of E_2 and HH$_1$.

Additional 1D transitions (e_2-hh_2, e_2-lh_2) would allow a direct quantitative measurement of minigap amplitudes.[11] They are, however, not resolved, probably because of the presence of the continuum of E_1.

VIII. PHOTOLUMINESCENCE LINEAR POLARIZATION

We analyze here the two photoluminescence linear polarization features labeled (i) and (ii) in Fig. 6.

Qualitatively, the origin of the negative PL LPR for small-**k** transitions [feature (i) in Fig. 6] is similar to that of the e_1-hh_1 PLE transition in PLE in undoped LSL's.[11] It is induced by the mixing between **k**$\simeq 0$ conduction states with **k**$\simeq(\pm 2\pi/L_x,0)$ states induced by 1D periodic confinement. However, the description of hole states cannot be limited to a free-electron model, since the associated PL LPR (-7%, neglecting static screening effects) clearly underestimates the experimental value (-18%). We rather describe holes as anisotropically localized states:

$$\Psi_{loc}(\mathbf{k}) \propto \exp\left(-\frac{k_x^2}{\Delta^2 k_x} - \frac{k_y^2}{\Delta^2 k_y}\right).$$

Using $\Delta k_x=0.035$ Å^{-1}, $\Delta k_y=0.013$ Å^{-1}, and $2V_{1D}=20$ meV, this model leads to a -17% PL LPR value for zone-center transitions, which falls in quantitative agreement with experimental data. We stress that even if a quantitative agreement is only reached within a localized hole level model, the physical origin of the negative LPR of zone-center transitions is in any case due to the quantum mixings in the LSL conduction band: a pure 2D **k**=0 conduction
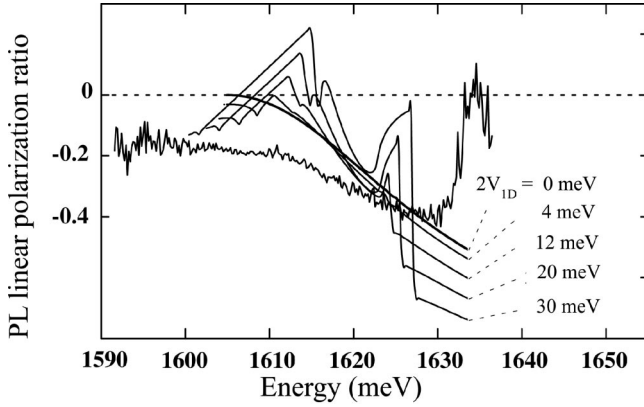
FIG. 9. PL linear polarization spectrum of sample B at 2 K (from Fig. 6). Solid lines refer to a fit with a localized hole model and a 1D confinement of amplitude V_{1D}.

state would give no optical anisotropy when recombining with Ψ_{loc} even with $\Delta k_x \neq \Delta k_y$. This means that the negative polarization of zone-center PL transitions [feature (i) in Fig. 6] fully originates in the periodicity of the LSL quantum confinement.

For higher wave-vectors transitions, the conduction-band structure becomes 2D like, so that the observed enhancement of the PL LPR [feature (ii) in Fig. 6] corresponds to another mechanism. To understand it, we calculated in Fig. 9 the PL LPR expected for 2D electrons ($2V_{1D}=0$ meV) recombining onto anisotropically localized holes. As explained above, $\mathbf{k}=0$ optical transitions remain isotropic despite the hole localization anistropy, but a negative PL LPR component develops with energy as valence-band mixing effects gradually take place outside the Brillouin zone center.[21] This is in good agreement with experimental data and suggests that the PL LPR enhancement for high wave-vector transitions is fully due to the localization anistropy of valence holes. We also propose in Fig. 9 a more complete calculation of the PL LPR including the LSL periodic confinement potential in the conduction band ($V_{1D} \neq 0$). With increased V_{1D} values, one recovers the negative PL LPR characteristic of zone-center optical transitions. It is remarkable that the calculated LPR shape then gets structured at higher wave vectors, due to the presence of conduction-band minigaps. This is not reflected by experiments, but is obviously related to the absence of Van Hove singularities in the PL spectrum, which we already discussed. Nevertheless, the envelope of the calculated PL LPR curves is preserved while increasing V_{1D}, so that the experimental increase of PL LPR at high wave vectors can be reasonably attributed to the anisotropy of localization of valence holes in LSL's.

To confirm this experimentally, we show in Fig. 10 the evolution of PL and PL LPR spectra with temperature. By raising the laser power, we obtain effective electronic temperatures up to 40 K (measured by the PL slope in logarithmic scale above E_F). For such temperatures, the electron gas distribution is quite unchanged ($E_F/k \gg 40$ K), so that the PL LPR evolution is only sensitive to the distribution of the photocreated holes. The small wave-vector PL LPR component faintly changes with temperature, while the high wave-
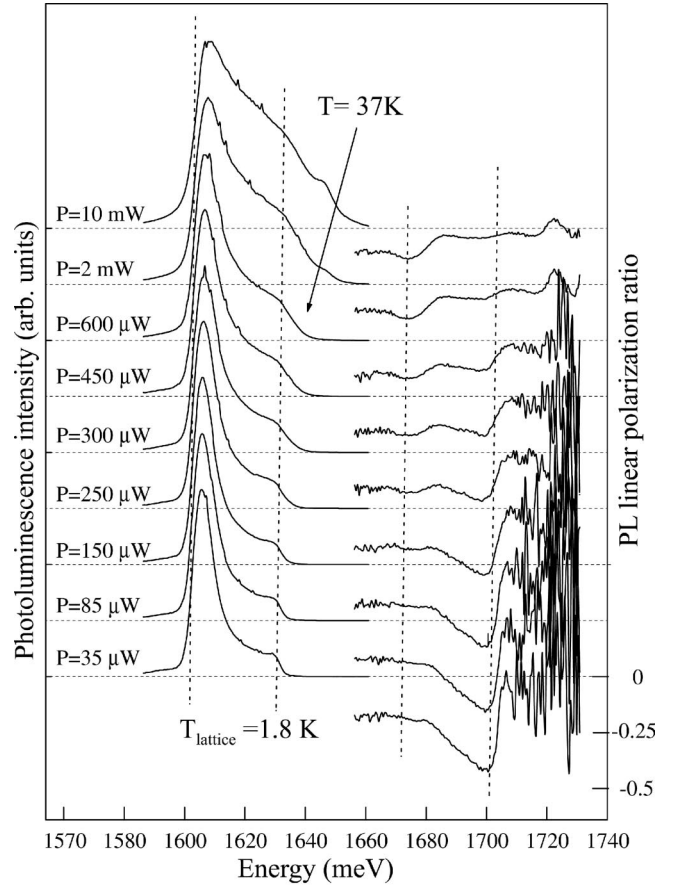

FIG. 10. Temperature evolution of the PL (left) and PL LPR (right) spectra of sample B for $N\varepsilon=0$. The temperature is tuned by raising the illumination power. PL LPR spectra are blueshifted by 70 meV for sake of clarity. Dotted lines are a guide to the eye for the two PL LPR components at small and high wave vectors.

vector contribution almost disappears for $T \simeq 40$ K. This demonstrates that the latter comes from the localization of holes—suppressed at 40 K—while the former originates in the conduction-band periodic couplings induced by the LSL and thus remains weakly affected by changes in the hole distribution. The two different physical origins of PL LPR components (i) and (ii) in Fig. 6 are thus distinguished experimentally.

IX. LINEAR DEPOLARIZATION AT THE PHOTOLUMINESCENCE FERMI EDGE

We now describe the optical processes in the spectral range of the PL Fermi-level transitions. They correspond to the linear depolarization feature labeled (iii) in Fig. 6, where both PL and PLE get depolarized within a few meV above the PL Fermi edge. We analyze this feature and show that it allows one to understand the physical nature of PL and PLE processes within this spectral range.

The depolarization feature (iii) is represented for both samples B and A in Figs. 11 and 12, together with the corresponding PL and PLE data in linear and logarithmic scales. It is remarkable that both PL and PLE linear polarization
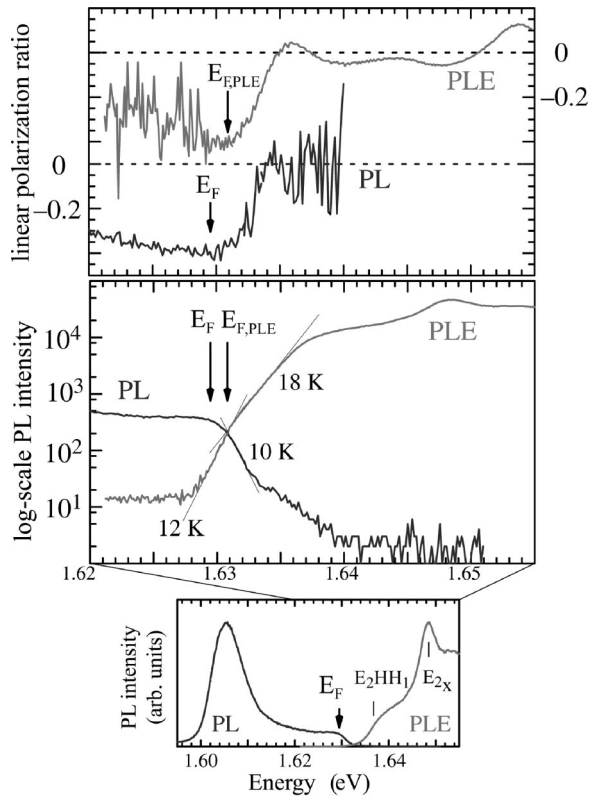
FIG. 11. Bottom: 1.8 K PL and PLE spectra of sample B for $N\varepsilon = 0$. Fermi-level transitions are positioned in PL from magneto-optical measurements. Top: same PL and PLE data in logarithmic scale plotted around Fermi-level transitions, together with the PL and PLE LPR spectra. The blueshift between PL and PLE LPR evidences a 1.4 meV Stokes shift, visible between PL and PLE Fermi-level transitions at E_F and $E_{F,PLE}$.
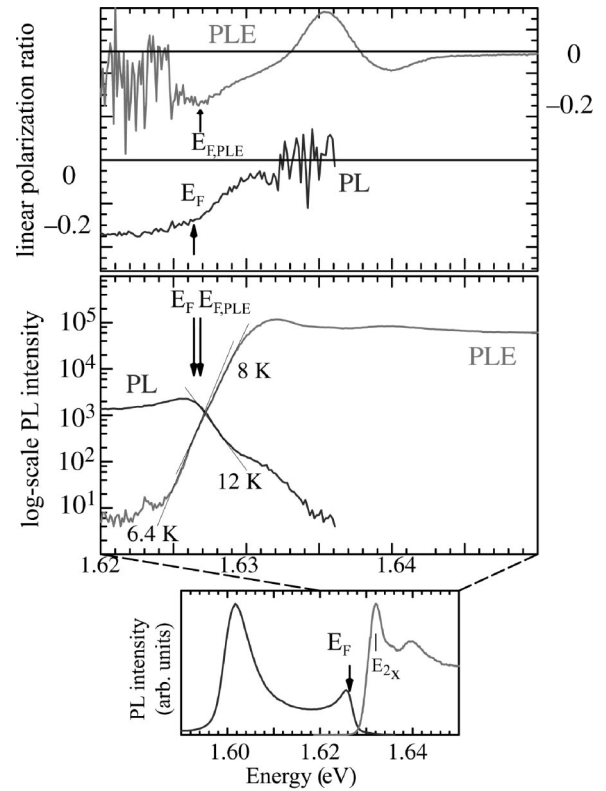

FIG. 12. Same figure for sample A. The pronounced Fermi-edge singularity seen in PL is due to the proximity of the second subband excitonic resonance E_{2_X} 6.5 meV above E_F. It modifies the PL and PL LPR shapes around PL Fermi-level transitions and the logarithmic-scale PL and PLE slopes compared to sample B (see text).

superimpose onto each other in a few meV spectral range above PL Fermi-level transitions, apart from a small ($\lesssim 2$ meV) energy shift, which we will later attribute to a Stokes shift. This occurs while PL and PLE signals have totally different variations with energy in this spectral range. Also, it remains valid for both samples A and B, although their LPR signals are quite different due to the proximity of E_{2_X} above PL Fermi-level transitions in the case of sample A. These two points demonstrate experimentally that the optical absorption (PLE) and emission (PL) processes are identical around the DEG Fermi level.

Given the analysis of the previous section, the PL depolarization above E_F can be understood as follows. If we assume that the DEG is at a temperature $T = 0$ K, PL transitions with energies higher than E_F require valence states closer to the valence-band edge, i.e., less localized, as depicted in Fig. 13. Thus, the PL spectrum above E_F is a spectroscopic probe of the valence-band tail of localized states. This explains the gradual depolarization in PL above E_F, because more delocalized LSL valence-band states are more isotropic. Also, fully depolarized transitions occur $\simeq 4$ meV above Fermi-level PL transitions, which falls in good agreement with the $\simeq 40$ K temperature required to suppress the high wave-vector LPR component (Fig. 10).

The same explanation in terms of localized valence states

applies for the PLE transitions in the LPR depolarization spectral range. This identifies the nature of the PLE transitions below the threshold for direct optical transitions at k_F (labeled as E_1HH_1 in Fig. 4) and shows that indirect optical processes dominate in this spectral range where direct transitions are prohibited due to the Pauli exclusion principle. The correspondence between PL and PLE processes is illustrated in Fig. 13. It shows that in the case of PLE, the absorption directly reflects the exponential density of states of the valence-band tail. This is not true, however, for PL transitions, where the effective population of the valence-band tail by photocreated carriers has to be taken into account. This dissymmetry is evidenced by logarithmic-scale PL and PLE data (Fig. 11): PLE and PL indeed display linear behaviors, but with different slopes, of respective temperatures $T = 18$ and 10 K for sample B.[28] From these PLE logarithmic scale slopes, one thus measures a characteristic localization energy $E_c \simeq 1.5$ meV for the valence-band tail. The value fairly agrees with the estimation (0.8 meV) from the 2D localization model, with a greater experimental value in LSL's probably related to the additionnal step-array disorder in the heterostructure.[17] The logarithmic scale slope difference between PL and PLE data would correspond to a population temperature $T = 6.5$ K of valence-band carriers within the localization band tail. However, this picture is not correct strictly speaking, because photocreated valence-band carriers
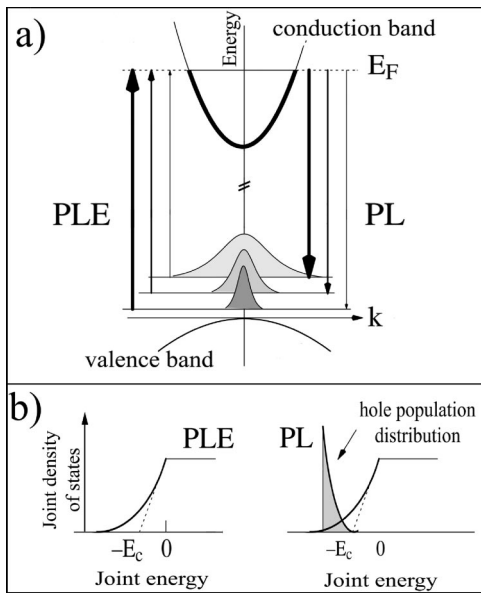
FIG. 13. (a) PL (right) and PLE (left) optical processes for transitions with energies above the Fermi level. The conduction-band DEG and the localized levels of the valence-band tail are represented with different energy scales. Bold and fine arrows are used to sketch the variations of oscillator strengths. (b) Joint density of states for the conduction and valence bands with the energy reference set to Fermi-level PL transitions. The tail of localized valence states is directly probed by PLE measurements (left), while PL experiments also depend on the actual population of the localized states.

probed in PL transitions are most likely out of thermal equilibrium, as can be seen from the energy shift ($\simeq 1$–2 meV) between PL and PLE LPR depolarization features in Figs. 11 and 12. It corresponds to a Stokes shift, PL transitions probing only valence holes having relaxed on lowest-energy potential fluctuations, while the PLE probes the spatial average of all localized states.

We finally focus on the PLE signal below the onset of the LPR depolarization at E_F. Logarithmic-scale PLE plots show a clear slope change at E_F for both samples B and A (12–18 K transition in Fig. 11 and 6.4–8 K transition in Fig. 12). Again, one sees that the PLE LPR mimics the PL LPR for this spectral range below E_F. This identifies the valence states involved in the PLE below E_F as the localized states involved in PL at E_F. Therefore, the PLE signal below E_F can be attributed to the thermal absorption in empty DEG states below E_F. From the logarithmic-scale PLE slope of sample B, one estimates an effective DEG temperature $T = 12$ K, quite above the helium bath temperature $T = 1.8$ K, but typical of a two-dimensional degenerate electron system under optical excitation.[14]

X. CONCLUSION

Optical experiments performed on remotely doped LSL's show that substantial information can be acquired about electronic states in 1D DEG's. We showed that LSL PL properties are governed by the quantum mixings induced by the LSL periodic potential, but also by the anisotropic localization of minority carriers, with extensions of 600 and 200 Å along and orthogonal to the QWR axis. We demonstrated that the two effects can be distinguished experimentally by the temperature dependence of photoluminescence linear polarization spectra. Moreover, thanks to the regime of anisotropically localized valence holes, we proved able to unambiguously identify the emission and absorption processes around Fermi-level transitions by a detailed analysis of PL and PLE LPR spectra. This description in terms of Fermi-level electrons recombining onto the tail of localized valence states extends to other degenerate electron systems in presence of disorder such as $Al_xGa_{1-x}As$ quantum wells.

*Electronic address: melin@isen.iemn.univ-lille1.fr

†Present address: Optoplus, Alcatel R&I, Route de Nozay, F-91460 Marcoussis, France.

[1] *Low-Dimensional Structures Prepared by Epitaxial Growth and Regrowth on Patterned substrates*, Vol. E298 of *NATO Advanced Study Institute*, Series E, edited by K. Eberl, P.M. Petroff, and P. Demeester (Kluwer Academic, Dordrecht, 1995).

[2] See, e.g., F. Rossi, G. Goldoni, and E. Molinari, Phys. Rev. Lett. **78**, 3527 (1997) and references therein.

[3] See, e.g., P. Nozières, J. Phys. I **4**, 1275 (1994).

[4] J. Bloch, U. Bockelmann, and F. Laruelle, Europhys. Lett. **28**, 501 (1994).

[5] F. Zwick, S. Brown, G. Margaritondo, C. Merlic, M. Onellion, J. Voit, and M. Grioni, Phys. Rev. Lett. **79**, 3982 (1997).

[6] A. Pinczuk, J. Shah, R.C. Miller, A.C. Gossard, and W. Wiegmann, Solid State Commun. **50**, 735 (1984).

[7] F. Perez, B. Jusserand, and B. Etienne, Phys. Rev. B **60**, 13 310 (1999).

[8] R. Ambigapathy, I. Bar-Joseph, D.Y. Oberli, S. Haacke, M.J. Brasil, F. Reinhardt, E. Kapon, and B. Deveaud, Phys. Rev. Lett. **78**, 3579 (1997).

[9] P.M. Petroff, A.C. Gossard, and W. Wiegmann, Appl. Phys. Lett. **45**, 620 (1984); J.M. Gaines, P.M. Petroff, H. Kroemer, R.J. Simes, R.S. Geels, and J.H. English, J. Vac. Sci. Technol. B **6**, 1378 (1988).

[10] R. Dingle, H.L. Störmer, A.C. Gossard, and W. Wiegmann, Appl. Phys. Lett. **33**, 665 (1978).

[11] T. Mélin and F. Laruelle, Phys. Rev. Lett. **81**, 4460 (1998).

[12] F. Petit, L. Sfaxi, F. Lelarge, A. Cavanna, M. Hayne, and B. Etienne, Europhys. Lett. **38**, 225 (1997).

[13] T. Mélin and F. Laruelle, Phys. Rev. Lett. **76**, 4219 (1996).

[14] T. Mélin and F. Laruelle, Phys. Rev. Lett. **85**, 852 (2000).

[15] T. Mélin and F. Laruelle, following paper, Phys. Rev. B **65**, 195303 (2000).

[16] F. Lelarge, Z.Z. Wang, A. Cavanna, F. Laruelle, and B. Etienne, Europhys. Lett. **39**, 97 (1997).

[17] F. Lelarge, F. Laruelle, and B. Etienne, Europhys. Lett. **40**, 213 (1997).

[18] B. Etienne, F. Laruelle, W. Wang, L. Sfaxi, F. Lelarge, F. Petit, T. Mélin, and A. Cavanna, Semicond. Sci. Technol. **11**, 1535 (1996).

[19] T. Mélin and F. Laruelle, Surf. Sci. **361/362**, 762 (1996).

[20] T. Mélin, Ph.D. thesis, Ecole Polytechnique, 1998.

[21] See, e.g., G. Bastard, *Wave-Mechanics Applied to Semiconductor Structures* (Les Editions de Physique, Les Ulis, France, 1988).

[22] S.K. Lyo, E.D. Jones, and J.F. Klem, Phys. Rev. Lett. **61**, 2265 (1988).

[23] D. Gammon, E.S. Snow, and D.S. Katzer, Surf. Sci. **361/362**, 814 (1996); F. Vouilloz, D.Y. Oberli, S. Wiesendanger, B. Dwir, F. Reinhardt, and E. Kapon Phys. Status Solidi A **164**, 259 (1997); J. Bellessa, V. Voliotis, R. Grousson, X.L. Wang, M. Ogura, and H. Matsuhata, *ibid.* **164**, 273 (1997).

[24] Piet van Mieghem, Rev. Mod. Phys. **64**, 3 (1992); B.I. Halperin and M. Lax, Phys. Rev. **148**, 722 (1967).

[25] See, e.g., J.W.G. Wildöer, L.C. Venema, A.G. Rinzler, R.E. Smalley, and C. Dekker, Nature (London) **391**, 59 (1998).

[26] P. Denk and J.L. Pélouard, Phys. Rev. B **63**, 041304 (2001).

[27] F. Rossi and E. Molinari, Phys. Rev. Lett. **76**, 3642 (1996).

[28] In sample A, the PL and PLE oscillator strengths cannot be taken as constant around Fermi-level transitions. This is due to the presence of a strong Fermi-edge singularity around E_F. It increases the PL and PLE oscillator strengths with energy and reduces the PLE apparent logarithmic-scale slope ($T = 8$ K) compared to sample B, while a $T \simeq 5$ K effective temperature for valence carriers accounts for the observed PL logarithmic-scale slope ($T = 12$ K).